IMPACTX: An X-ray Spectral Model for Polar Dust and Clumpy Torus

Kanta Fujiwara [ID],[1] Yoshihiro Ueda [ID],[1] Shoji Ogawa [ID],[2] Yuya Nakatani [ID],[1] and Ryosuke Uematsu [ID][1]

[1]*Department of Astronomy, Kyoto University, Sakyo-ku, Kyoto, Japan*

[2]*Institute of Space and Astronautical Science (ISAS), Japan Aerospace Exploration Agency (JAXA) 3-1-1 Yoshinodai, Chuo-ku, Sagamihara, Kanagawa, Japan*

ABSTRACT

We construct a generic X-ray spectral model for the reflection component from the clumpy torus and dusty gas in the polar region (polar dusty gas) in an active galactic nucleus (AGN), designated as Inclusive spectral energy distribution Model of Polar dust And Clumpy Torus for X-ray (IMPACTX). To calculate the spectra, we utilize the Monte-Carlo based, 3-dimensional radiative transfer code SKIRT. The adopted geometry is the same as that of the IMPACT model (Ogawa et al. in prep.), consisting of a clumpy torus defined by Nenkova et al. (2008) and paraboloid-shell polar dusty gas launched at the inner radius of the torus. We discuss the dependence of the X-ray spectrum on geometrical parameters in comparison with the conventional torus-only model (XCLUMPY). As an example, we have simultaneously applied the IMPACTX and IMPACT models to the X-ray and infrared spectra of the nearby Seyfert 2 galaxy NGC 4388, and have found a solution that can well reproduce both spectra. This demonstrates the importance of using both X-ray and infrared data to constrain the nuclear structure of an AGN.

1. INTRODUCTION

In the present universe, the mass of the stellar bulge of a galaxy and that of the supermassive black hole (SMBH) in its center are tightly correlated, despite their large difference in spatial scale by $\sim$10 orders of magnitude (Kormendy & Ho 2013). The co-moving density of star formation rate (e.g., Madau & Dickinson 2014) and that of mass accretion rate onto SMBHs (e.g., Ueda et al. 2014; Aird et al. 2015) show overall similar cosmological evolution, peaking at $z \sim 2$. These facts lead to the idea of "co-evolution" of galaxies and SMBHs. Active galactic nuclei (AGNs) are the key object to investigate the physical processes of galaxy-SMBH co-evolution, because it is the site where mass fed by the host galaxy is accreted by the SMBH and also, because they are bright, AGNs allow you to actually observe SMBHs. To understand the mass transfer processes, it is critical to constrain the nuclear structure of AGNs.

In the classical unified model (Antonucci & Miller 1985; Awaki et al. 1991) of AGNs, the SMBH and accretion disk are surrounded by "dusty torus" (see Ramos Almeida & Ricci (2017) for a review), which blocks the observer's line-of-sight toward the SMBH when viewed edge-on. This model is successful to explain many basic aspects of AGNs, particularly the observed differences between type-1 (unobscured) and type-2 (obscured) AGNs. Recent observational and the-

oretical studies have revealed that the nuclear structure is far more complex, however. Mid-infrared (IR) interferometry observations of nearby AGN revealed that a significant part of the dust emission extends in the polar direction, instead of the equatorial direction where the classical torus resides (e.g. Jaffe et al. 2004; Hönig et al. 2006, 2012, 2013; Tristram et al. 2014; López-Gonzaga et al. 2014, 2016; Leftley et al. 2018; Asmus 2019; Isbell et al. 2022, 2025; see Burtscher et al. (2016) for a review). This structure is often called "polar dust" (in this paper we refer to it as "polar dusty gas" because the total mass is dominated by gas accompanying dust that emits mid-IR radiation). In fact, theories predict the presence of a radiation-driven outflow launched at the innermost region (Schartmann et al. 2014; Wada et al. 2016), which most likely corresponds to the observed polar dusty gas. On the basis of these results, Ogawa et al. (2021) propose an updated unified scheme where the presence of polar dusty gas is universal, to consistently explain X-ray and infrared properties of AGNs.

Infrared and X-ray spectra provide us with complementary information on the torus structure including polar dusty gas. Infrared emission directly traces AGN-heated dust, whereas X-rays trace all matter including gas and dust through absorption and/or reflection signals. It is important to have theoretical spectral models for AGNs, which allow one to directly compare with the observations. Before the discovery

of polar dusty gas, models took into account only the classical torus (i.e., without polar dusty gas) both in the infrared band (e.g., Krolik & Begelman 1988; Pier & Krolik 1992; Efstathiou et al. 1995; Siebenmorgen et al. 2005; Fritz et al. 2006; Nenkova et al. 2008a,b; Schartmann et al. 2008; Hönig & Kishimoto 2010; Stalevski et al. 2012, 2016) and in the X-ray band (e.g., Murphy & Yaqoob 2009; Ikeda et al. 2009; Paltani & Ricci 2017; Baloković et al. 2018 for smooth tori; e.g., Furui et al. 2016; Tanimoto et al. 2019, and Buchner et al. 2019 for clumpy tori. Given the fact that the polar dusty gas is ubiquitous in AGNs, these models must be updated by including the contribution from it.

Ricci & Paltani (2023) also point out the importance of considering dusty media in high-resolution X-ray spectroscopy, which produces complex near-edge X-ray absorption fine structures.

In the infrared band, Hönig & Kishimoto (2017) calculated infrared spectra from the torus and polar dusty gas using a radiative transfer model called CAT3D-WIND. Stalevski et al. (2017, 2019) studied the infrared spectrum from polar dusty gas in Circinus Galaxy, using the SKIRT code (Baes et al. 2011; Camps & Baes 2015; Camps & Baes 2020; Van der Meulen et al. 2023). Recently, Ogawa et al. (in preparation. hereafter Paper I) have constructed a more generic infrared spectral model using SKIRT. They are able to well reproduce the infrared spectra of 28 nearby AGNs whose nuclei are separated by ground-based, high angular-resolution mid-infrared imaging (Ichikawa et al. 2015; García-Bernete et al. 2019). This model, designated as Inclusive spectral energy distribution Model of Polar dust And Clumpy Torus (IMPACT), adopt the same geometry as in the CLUMPY (Nenkova et al. 2008a,b) and XCLUMPY (Tanimoto et al. 2019) models for the torus, and the paraboloid-shell geometry for the polar dusty gas, which is similar to hourglass-like curved shell suggested by Wada et al. (2016) and Kudoh et al. (2023).

In the X-ray bands, several authors studied the reflection component from the polar dusty gas. Liu et al. (2019) simulated the reflection spectra from the clumpy torus and clumpy polar dusty gas, and suggested that fluorescent lines below 3 keV may significantly come from the polar dusty gas. McKaig et al. (2022) also investigated the X-ray spectral contribution of polar dust with different geometries. They also reported that optically thin polar dust increases the scattering component at the low energy side of the X-ray spectrum. Andonie et al. (2022) presented an X-ray spectral model specifically for Circinus Galaxy, assuming a more complex geometry, including the accretion disk, flared disks, broad line region, torus, and polar dusty gas. These works, though novel, assumed very simplified geometry for the polar dusty gas (hollow cone or filled cone), which may not be compatible with the infrared SED (Stalevski et al. 2019, Paper I). In addition, the calculations were performed only within a limited parameter range and hence cannot be applied to many objects.

In this paper, we construct a more generic X-ray spectral model from the clumpy torus and polar dusty gas that is applicable to any objects, designated as Inclusive SED Model of Polar dust and Clumpy Torus for X-ray (IMPACTX). We adopt the same geometry as in the IMPACT model (Paper I). This enables us to simultaneously analyze the X-ray and infrared spectra under a common assumption for the geometry. The structure of this paper is as follows. Section 2 describes the adopted geometry of the torus and polar dusty gas, and the details of Monte Carlo simulations. In section 3, we report the basic properties of our model, and discuss the effects of including the polar dusty gas with various geometrical parameters by comparison with the XCLUMPY model. In section 4, we simultaneously analyze the X-ray spectra and infrared SED of the nearby Seyfert-2 galaxy NGC 4388, using IMPACTX and IMPACT, respectively. Throughout the paper, errors correspond to the 90% confidence region for a single parameter.

2. SIMULATIONS

2.1. *Torus Geometry*

In our model, we assume a clumpy torus, which is considered to be more realistic case than a smooth torus with a uniform density (for a brief review on this issue, see e.g., Tanimoto et al. 2019). The torus geometry is the same as in the CLUMPY (Nenkova et al. 2008a,b) and XCLUMPY (Tanimoto et al. 2019) models. It consists of randomly placed clumps with a fixed size (the radius of each clump; $R_{\rm clump}$ is 0.002 pc) according to a power-law distribution in the radial direction and a Gaussian distribution in the angular direction. The number density function $d(r, \theta, \phi)$ is represented in the spherical coordinate system (where r is radius, θ is polar angle, and ϕ is azimuth) as:

$$d(r, \theta, \phi) = N \left(\frac{r}{r_{\rm in}} \right)^{-q} \exp \left(-\frac{(\theta - \pi/2)^2}{\sigma^2} \right). \quad (1)$$

where N is the normalization, $r_{\rm in}$ is the inner radius of the torus, q is the index of the radial density profile, and σ represents the torus angular width.

The normalization N is related to the number of clumps along the equatorial plane $N_{\rm clump}^{\rm Equ}$ as

$$N_{\rm clump}^{\rm Equ} = \int_{r_{\rm in}}^{r_{\rm out}} d\left(r, \frac{\pi}{2}, 0 \right) \pi R_{\rm clump}^2 dr, \quad (2)$$

$$N = \frac{(1 - q) N_{\rm clump}^{\rm Equ}}{\pi R_{\rm clump}^2 r_{\rm in}^q (r_{\rm out}^{1-q} - r_{\rm in}^{1-q})}. \quad (3)$$

where $r_{\rm in}$ and $r_{\rm out}$ are inner and outer radii of the torus.

Furthermore, the hydrogen column density along the equatorial plane $(N_{\mathrm{H}}^{\mathrm{Equ}})$ is expressed using hydrogen number density n_{H} by the following equation.

$$N_{\mathrm{H}}^{\mathrm{Equ}} = \frac{4}{3} R_{\mathrm{clump}} N_{\mathrm{clump}}^{\mathrm{Equ}} n_{\mathrm{H}} \qquad (4)$$
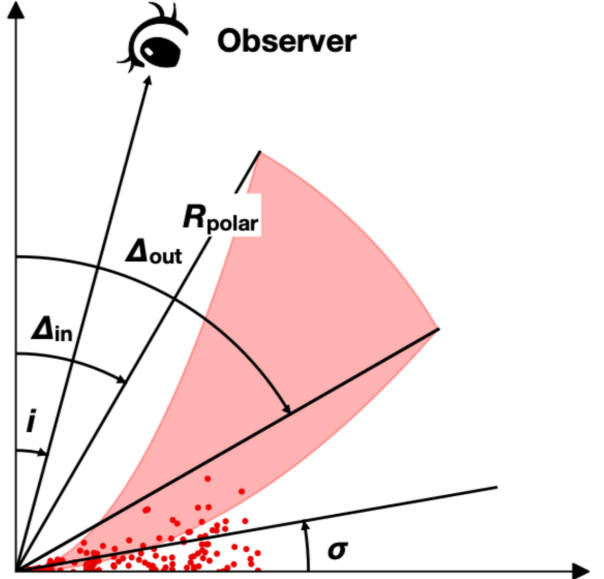
We fix $N_{\mathrm{clump}}^{\mathrm{Equ}}$ to 10, $q = 0.5$, $r_{\mathrm{in}} = 0.05$ pc and $r_{\mathrm{out}} = 1.00$ pc as in the XCLUMPY model (Tanimoto et al. 2019). Thus, the free parameters are the angular width of the torus (σ) and the hydrogen column density along the equatorial plane $(N_{\mathrm{H}}^{\mathrm{Equ}})$.

2.2. Geometry of Polar Dusty Gas

For the polar dusty gas, we adopt the same paraboloid-shell geometry (Figure 1) as that in the IMPACT model (Paper I). The shape is similar to hourglass-like curved shell suggested by Wada et al. (2016) and Kudoh et al. (2023) based on their three dimensional radiation-hydrodynamic simulations. It has 5 geometric parameters: radial extent of the paraboloid shell R_{Polar}, half opening angle of the inner paraboloid Δ_{in}, that of the outer paraboloid Δ_{out}, and the inner radius of the paraboloid shell r_{in}. In this work, we fix Δ_{out} to $\Delta_{\mathrm{in}} + 30$ deg, which well reproduces typical IR SEDs of AGNs (Paper I), and r_{in} to 0.05 pc, for consistency with the torus inner radius adopted in XCLUMPY. For simplicity, we assume uniform density distribution of gas and dust as in the IMPACT model. To make the spectral model "scale-free", i.e., invariant for any choice of r_{in}, which depends on the bolometric luminosity of AGN (Paper I), we define the radial-thickness parameter of the paraboloid $Y_{\mathrm{Polar}} = R_{\mathrm{Polar}}/r_{\mathrm{in}}$ and the hydrogen column-density parameter $N_{\mathrm{H}}^{\mathrm{Polar}} = R_{\mathrm{Polar}} \, n_{\mathrm{H}}^{\mathrm{Polar}}$ [1] where $n_{\mathrm{H}}^{\mathrm{Polar}}$ is the hydrogen number density. Thus, the free parameters specific to the polar dusty gas are Δ_{in}, Y_{Polar}, and $N_{\mathrm{H}}^{\mathrm{Polar}}$.

In this study, we restrict $N_{\mathrm{H}}^{\mathrm{Polar}} < 10^{23.5}$ cm^{-2}; otherwise the photoelectric absorption by the polar dusty gas becomes unrealistically large even in type-1 AGNs, which is contradictory to the observations (Liu et al. 2019). Observational studies have shown that the extent of polar dust ranges from 10 to several hundred parsecs (e.g. Bock et al. 2000, Radomski et al. 2003, Packham et al. 2005, Asmus et al. 2016, Isbell et al. 2025). Thus, we limit $Y_{\mathrm{Polar}} < 2000$, corresponding to $R_{\mathrm{Polar}} < 800$ pc for $r_{\mathrm{in}} = 0.4$ pc, the dust sublimation radius for a typical bolometric luminosity of 10^{45} erg s^{-1} (Nenkova et al. 2008a,b).

2.3. Material Properties and Physical Processes

Figure 1. Cross-section view of the torus and polar dusty gas (taken from Figure 1 of Paper I).

To produce the X-ray spectral model reflected from the torus and polar dusty gas, we utilize the Monte-Carlo 3-dimensional simulation code SKIRT (Baes et al. 2011; Camps & Baes 2015; Camps & Baes 2020; Vander Meulen et al. 2023; Vander Meulen et al. 2024), which can calculate over a wide range of wavelengths from X-rays to radio waves. We assume that all matter in the torus and polar dusty gas is neutral (not ionized) gas. For simplicity, the effect of dust on the X-ray spectra, such as the X-ray absorption fine structure, is ignored [2]. The physical processes considered are photoelectric absorption, electron scattering, and fluorescence emission lines. In SKIRT, the photoelectric-absorption cross sections by Verner & Yakovlev (1995) and Verner et al. (1996) are adopted, and scattering by electrons bound in gas is taken into account. For our model calculation, we assume the solar abundances by Lodders et al. (2009).

In our SKIRT simulations, we adopt a cubic spatial domain extending $4 \times R_{\mathrm{Polar}}$ pc in all three directions, discretized using an octree-based adaptive grid with a maximum subdivision level of 15, corresponding to a minimum cell size of ~ 0.0012 pc within the 40 pc simulation domain. This is finer than the diameter of the smallest structural elements in the model—the clumps (0.004 pc)—and is therefore adequate for resolving them. The spectral energy grid for the instruments is defined on a logarithmic scale, covering the range from 0.5 to 100 keV with 4000 grid points. The energy grid around 6.4 keV has a spacing of approximately 0.01 keV,

---

[1] Hereafter we simply refer to $N_{\mathrm{H}}^{\mathrm{Polar}}$ as the hydrogen column density (of the polar dusty gas), which is an effective value integrated along a straight line from the origin to R_{Polar} assuming a constant density.

[2] Nevertheless, we call this component as "polar dusty gas" throughout the paper, to distinguish it from ionized, dust-free gas in the polar region.

which provides sufficient spectral resolution for comparison with typical X-ray CCD observations. For each run, 5×10^6 photon packets are launched. The intrinsic photon spectrum is modeled by the form of $AE^{-\Gamma}\exp(-E/E_{\mathrm{cut}})$, where A is the normalization, Γ the photon index, and E_{cut} the high energy cutoff. The simulations were performed over the parameter grid summarized in Table 1.

3. RESULTS

We investigate the dependence of the reflected X-ray spectrum on the polar dusty gas parameters. Here we adopt the following default set of parameters, unless otherwise stated: $\log N_{\mathrm{H}}^{\mathrm{Torus}}/\mathrm{cm}^{-2} = 24.0$, $\sigma = 20.0°$, $\log N_{\mathrm{H}}^{\mathrm{Polar}}/\mathrm{cm}^{-2} = 21.5$, $\Delta_{\mathrm{in}} = 10.0°$, $Y_{\mathrm{Polar}} = 200$, $\Gamma = 1.8$, $E_{\mathrm{cut}} = 370$ keV. Figure 2 displays the images of the reflection components around 0.5 keV, 1.7 keV (including Si Kα), 3.0 keV, 6.4 keV (including Fe Kα), and 20.0 keV when the angle of inclination changes to 0°, 30°, 60°, 90°. As noticed, the emission around Si Kα (1.7 keV) is dominated by that from of the polar dusty gas at high inclination angles. By contrast, the emission around Fe Kα (6.4 keV) comes almost entirely from the torus. These results support the suggestion by Liu et al. (2019) that Si Kα / Fe Kα is a good indicator to search for objects with significant polar dusty gas. Figure 3 plots the total spectra including the direct component and the reflection components from the torus and polar dusty gas for $i = 10°$ (left) and $i = 80°$ (right). As noticed, in the face-on case, the direct component dominates over the reflected component, so that any enhancement of the polar dust reflection would be hardly detectable in actual observations. Hence, we hereafter focus on the edge-on case.

Figure 4 (left) plots the reflection spectra observed edge-on ($i = 80°$) with different half opening angles Δ_{in}. For comparison, the reflection spectrum only from the torus (without polar dusty gas), calculated using the XCLUMPY(SKIRT) model (Appendix B), is also plotted. As noticed, the flux at low energies (<5 keV) becomes larger when the polar dusty gas is present, confirming the results by Liu et al. (2019) and McKaig et al. (2022). The soft X-ray flux (<5 keV) decreases with Δ_{in}. This can be understood as follows. For the default parameter set, the polar dusty gas is optically thin. For photoelectric absorption at >0.5 keV, it basically produces unabsorbed scattered component by keeping the shape of the intrinsic power law component. The amount of this additional component is roughly proportional to the total number of electrons (hence hydrogen atoms) in the polar dusty gas that is not blocked by the optically thick torus when viewed from the central engine; hence, the soft X-ray flux decreases with Δ_{in} as the torus obscuration becomes more significant. Furthermore, a smaller Δ_{in} of the polar dust increases the solid angle subtended by the polar dust as viewed from the line of sight, which also contributes to the stronger reflected spectrum. Figure 4 (right) shows the dependence of the reflected X-ray spectrum at $i = 80°$ on the hydrogen column density of the polar dusty gas ($N_{\mathrm{H}}^{\mathrm{Polar}}$). The contribution of scattered X-rays from the polar dusty gas increases with $N_{\mathrm{H}}^{\mathrm{Polar}}$ in this range. It is notable that, as the density increases, the soft X-ray flux becomes more attenuated, due to self-absorption in the polar dusty gas. The trend is similar to that reported by Liu et al. (2019).

We investigate the relation between the fluxes of fluorescent emission lines and the polar-dusty-gas parameters in Figure 5. Here we consider fluorescent lines of O, Ne, Mg, Si, S, Ar, and Ca, because the effect by the polar dusty gas is important at low energies (<4 keV) as shown in Figure 4. As noticed, the line fluxes in the torus plus polar dusty gas case are always larger than those in the torus-only case. They increase with decreasing Δ_{in}, and with increasing $N_{\mathrm{H}}^{\mathrm{Polar}}$ except for oxygen and neon in the adopted range of $N_{\mathrm{H}}^{\mathrm{Polar}}$ values. This is because, similarly to the Compton scattered continuum, the fluorescent-line flux from the polar dusty gas should be roughly proportional to the total number of atoms in the volume irradiated by the intrinsic X-ray emission (i.e., that not blocked by the torus) unless the gas is optically thick for photoelectric absorption. In the high column density case ($N_{\mathrm{H}}^{\mathrm{Polar}}/\mathrm{cm}^{-2} = 22.5$), self-absorption within the polar dusty gas reduces the observed flux of the oxygen line (0.5 keV) and neon line (0.8 keV).
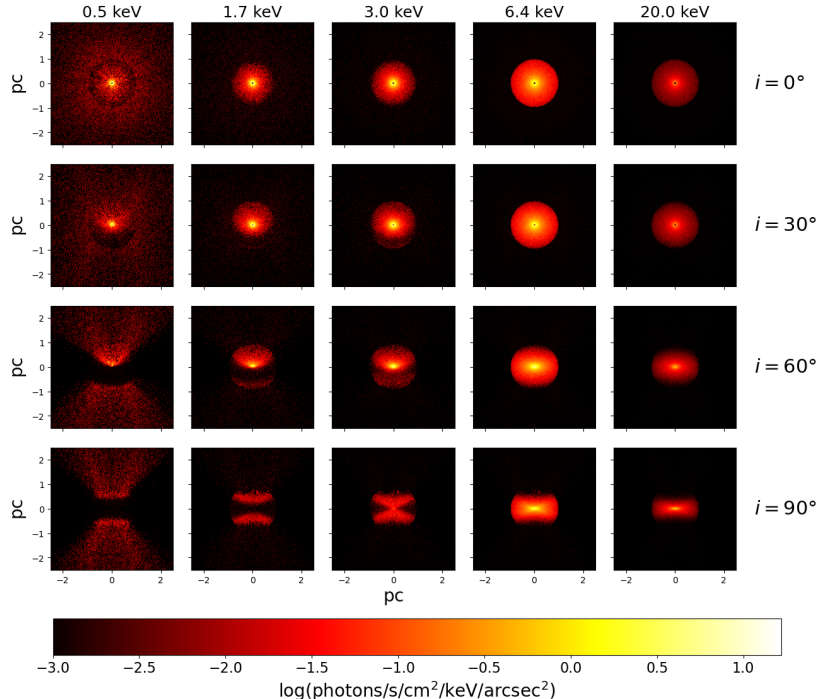
4. APPLICATION TO NGC 4388

As an example, we apply the IMPACT and IMPACTX models to NGC 4388, one of the closest ($z = 0.00842$) Seyfert 2 galaxies (Huchra et al. 1982) located at a distance of 18.0 Mpc (Sorce et al. 2014). This object is a member of the sample consisting of 28 AGNs analyzed by Ogawa et al. (2021) and Paper I, for which nuclear infrared SEDs obtained by high angular-resolution mid-infrared imaging are available (García-Bernete et al. 2019). It is X-ray bright, showing the brightest Fe Kα line among Compton-thin obscured AGNs (Fukazawa et al. 2011), and is a target of a XRISM observation in GO-1 (PI: Ueda). Thus, NGC 4388 is an ideal target to demonstrate the utility of our model.

We analyze the infrared SED of the nucleus compiled in Paper I, covering the 1–100 μm band. It consists of the photometric or spectroscopic data summarized in Table A1. Figure 6 plots the IR SED (including upper limits) as a function of wavelength. We utilize the same broadband X-ray spectrum reduced by Ogawa et al. (2021). It consists of the Suzaku/XIS and NuSTAR spectra observed in 2005 and 2013, covering the 0.5-10 keV and 8–75 keV bands, respectively. The observed spectra folded with the energy response

Table 1. Summary of Parameters

No.	Parameter	Grid	Units
(1)	σ	10, 20, 30	degree
(2)	$\log N_{\mathrm{H}}^{\mathrm{Equ}}$	23.5, 24.0, 24.5	cm^{-2}
(3)	Δ_{in}	10, 20, 30, 40	degree
(4)	Y_{Polar}	200, 2000	
(5)	$\log \mathrm{N}_{\mathrm{H}}^{\mathrm{Polar}}$	21.5, 22.0, 22.5, 23.0, 23.5	cm^{-2}
(6)	$Z(\mathrm{Fe})$	1.0, 1.5, 2.0, 2.5, 3.0	solar
(7)	i	65.0, 75.0, 85.0	degree

NOTE— (1) Half angular width of the torus. (2) Logarithm of the hydrogen column density of the torus along the equatorial plane . (3) Half opening angle of inner wall of the polar dusty gas. (4) Radial thickness parameter of the polar dusty gas ($R_{\mathrm{Polar}}/r_{\mathrm{in}}$). (5) Logarithm of the hydrogen column density of the polar dusty gas. (6) Abundance of Fe relative to hydrogen. (7) Inclination angle of the observer.
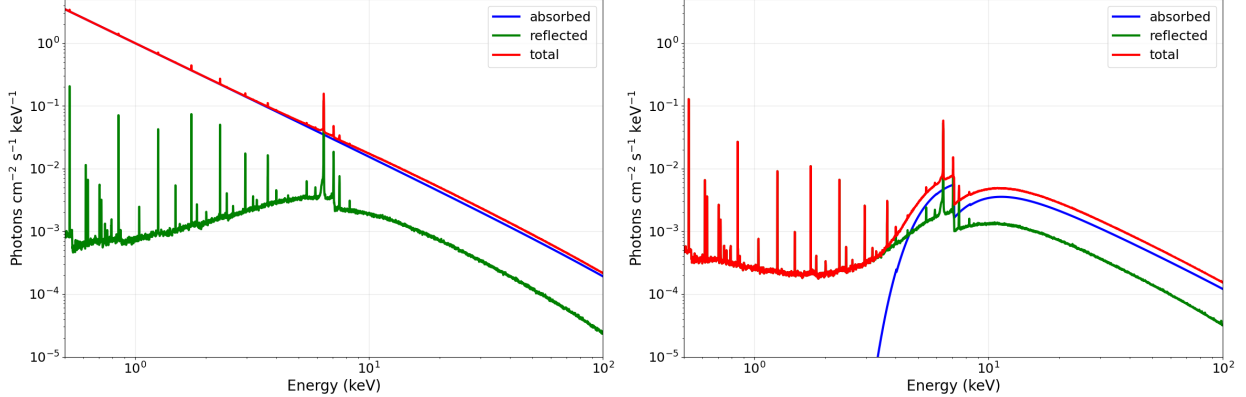
Figure 2. Simulated images of the torus plus polar dusty gas around 0.5 keV, 1.7 keV, 3.0 keV, 6.4 keV, 20.0 keV viewed at inclination angles of i = 0°, 30°, 60°, and 90° (from top to bottom). The color bar represents the photon flux density per arcsec^2. We adopt the following parameters: $\log N_{\mathrm{H}}^{\mathrm{Torus}}/\mathrm{cm}^{-2} = 24.0$, $\sigma = 20.0°$, $\Gamma = 1.8$, $E_{\mathrm{cut}} = 370$ keV, $\Delta_{\mathrm{in}} = 10.0°$, $Y_{\mathrm{Polar}} = 200$, and $\log N_{\mathrm{H}}^{\mathrm{Polar}}/\mathrm{cm}^{-2} = 21.5$.

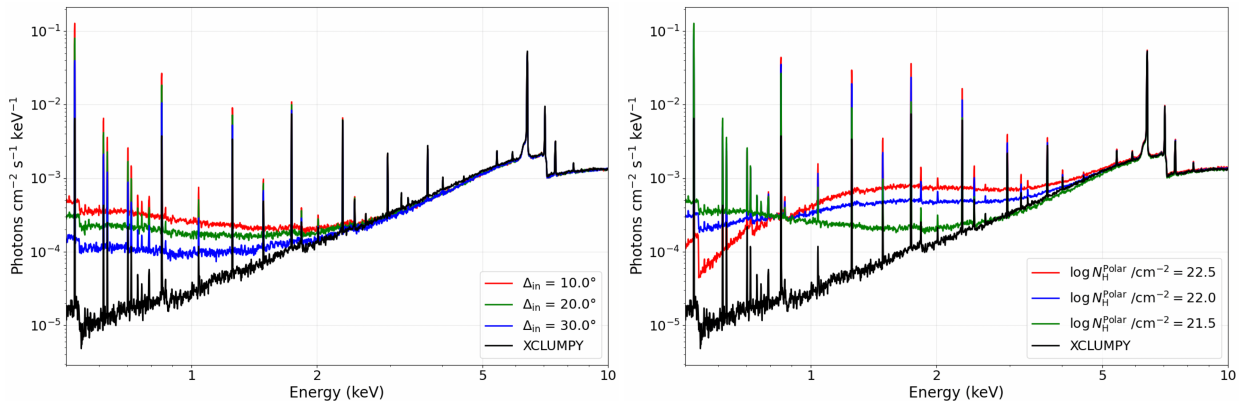are plotted in Figure 7 (a). The observation log is given in Table A2.

4.1. *Spectral Analysis*

In order to determine the AGN structure including the torus and polar dusty gas, the simplest way is to perform simultaneous fitting to the IR and X-ray spectra by leaving all geometrical parameters free at once. In practice, however, since the number of data points of the IR SED are much smaller than that of the X-ray spectra in our case, the obtained results may heavily depend on the X-ray data and constraints from
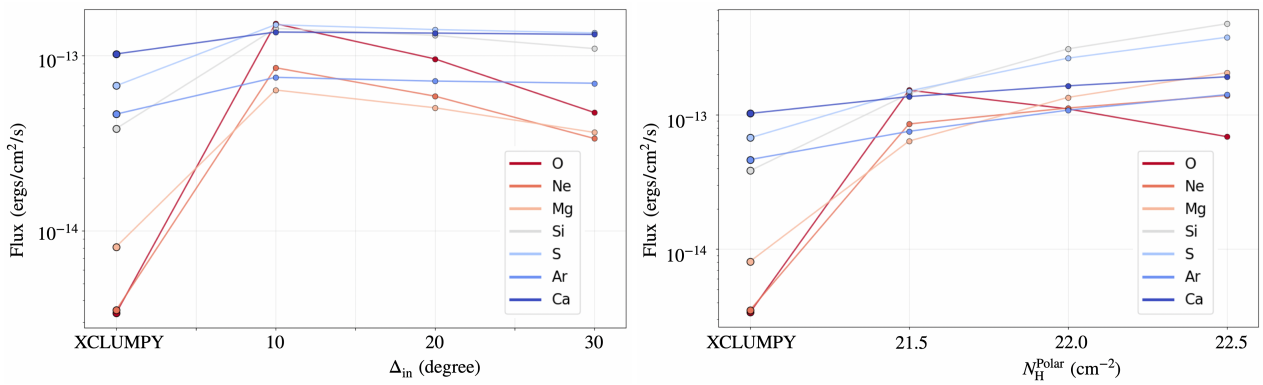
the IR data could not be well reflected. To avoid this situation, we take a step-by-step approach as described below. We recall that a large fraction of IR emission from an obscured AGN comes from the polar dusty gas (e.g. Hönig et al. 2006, 2012, 2013; Tristram et al. 2014; López-Gonzaga et al. 2014, 2016; Leftley et al. 2018; and Asmus 2019), whereas X-ray reflection component is dominated by that from the torus region except for extreme values of the number density and half opening angle (Figures 2 and 4).

Figure 3. Comparison of the reflection and direct components at $i = 10.0°$ (left) and at $i = 80.0°$ (right). We assume $\log N_H^{Torus}/cm^{-2} = 24.0$, $\sigma = 20.0°$, $\log N_H^{Polar}/cm^{-2} = 21.5$, $\Delta_{in} = 10.0°$, $Y_{Polar} = 200$, $\Gamma = 1.8$, and $E_{cut} = 370$ keV.

Figure 4. (Left) The X-ray reflection spectra observed edge-on ($i = 80°$) calculated for different half opening angles of the polar dusty gas. The red, green, and blue curves correspond to $\Delta_{in} = 10.0°$, $20.0°$, and $30.0°$, respectively, and the black one to the torus-only case. We assume $\log N_H^{Polar}/cm^{-2} = 21.5$, $Y_{Polar} = 200$, $\Gamma = 1.8$, and $E_{cut} = 370$ keV. (Right) Those for different effective hydrogen column densities of the polar dusty gas. The red, green, and blue curves correspond to $\log N_H^{Polar}/cm^{-2} = 22.5, 22.0$, and 21.5 respectively, and the black one to the torus-only case. We assume $\Delta_{in} = 10.0°$. The other parameters are the same as in the left panel.

Figure 5. (Left) The fluxes of fluorescent lines of O, Ne, Mg, Si, S, Ar, and Ca for different Δ_{in}. The leftmost one corresponds to the torus-only case. (Right) Those for different hydrogen column densities of the polar dusty gas. The leftmost one corresponds to the torus-only case. In both panels, we assume the default parameter set and $i = 80°$.

1. First we fit the X-ray spectra (0.5–75 keV) by ignoring the polar dusty gas, utilizing the XCLUMPY(SKIRT) model (Appendix B).

2. Next we fit the IR SED (1–100 μm) with the IMPACT model to constrain the polar-dusty-gas parameters by limiting the range of torus parameters within uncertainties estimated in the first step.

3. Finally, we fit the IR and X-ray spectra simultaneously with the IMPACT and IMPACTX models, respectively. Here we fix the parameters related to the polar dusty gas (Δ_{in}, Y_{Polar}, and $N_{\text{H}}^{\text{Polar}}$) at the best-fit values.

For the fitting, we utilize the XSPEC package (version 12.15.0) both for the IR and X-ray spectral analysis, by converting the units of Å to keV in the IR spectrum. In our analysis, we fix $E_{\text{cut}} = 370$ keV and $i = 70°$ from Ogawa et al. 2021, which are not well constrained from our data. We also limit $\Delta_{\text{in}} > 20°$, to make it consistent with the observed opening angle of the ionization cone in NGC 4388 (Gómez-Guijarro et al. 2017).

4.1.1. *IR SED Model*

The model use to fit the IR SED is represented as follows in the XSPEC terminology:

$$
\begin{aligned}
\text{model}_{\text{IR}} = \ &\text{zdust} * \text{zdust} \\
&* (\text{atable}\{\text{impact\_disk\_direct.fits}\} \\
&+ \text{atable}\{\text{impact\_disk\_scattered.fits}\} \\
&+ \text{atable}\{\text{impact\_dust\_direct.fits}\} \\
&+ \text{atable}\{\text{impact\_dust\_scattered.fits}\}) \quad (5)
\end{aligned}
$$

The two zdust terms represent dust extinction in our Galaxy and the host galaxy. The color excess $E(B-V)$ in the former is fixed at the total Galactic value determined from the dust map (Schlegel et al. 1998), whereas that in the latter is left free by adopting the extinction curve of Small Magellanic Cloud (SMC; Prevot et al. 1984), which is preferred to represent that in an AGN (e.g. Hopkins et al. 2004; Salvato et al. 2009; Bongiorno et al. 2012; Buat et al. 2021; Yamada et al. 2023). The first two atable terms represent the direct and scattered emission from the accretion disk, and the third and fourth ones the direct and scattered emission from the torus plus polar dusty gas. The geometrical parameters in these tables are all linked together.

4.1.2. *X-ray Spectral Model*

The X-ray spectral model is represented as follows in the XSPEC terminology:

$$
\begin{aligned}
\text{model}_{\text{X}} = \ &\text{const1*phabs} \\
&* (\text{const2*zphabs*cabs*zcutoffpl} \\
&+ \text{const3*zcutoffpl} + \text{atable}\{\text{impactx.fits}\} \\
&+ \text{zgauss} + \text{apec1} + \text{apec2})
\end{aligned}
$$

1. The const1 term is a cross-normalization constant to adjust small differences in the absolute flux calibration among different instruments. We set those of Suzaku/FIXIS and NuSTAR/FPM to unity as references. The phabs term represents the Galactic absorption, whose hydrogen column density is fixed at 2.87×10^{20} cm^{-2}, a value estimated by the method of Willingale et al. (2013).

2. The first term represents the transmitted component absorbed by the torus. The line-of-sight column density is determined by the torus parameters with this equation
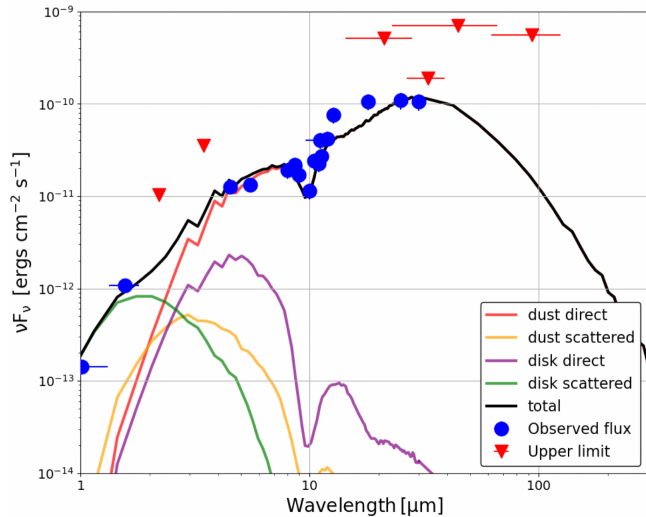
$$
N_{\text{H}}^{\text{LOS}} = N_{\text{H}}^{\text{Equ}} \exp\left(-\frac{(\theta - \pi/2)^2}{\sigma^2}\right). \quad (6)
$$

Note that the cabs model assumes free-electron scattering, whereas this work (SKIRT) assumes scattering by electrons bound to atoms. We confirm the difference in the total scattering cross section ($< 10\%$) does not affect our fitting results.

3. The second one is an unabsorbed scattered component from ionized gas in the polar region (i.e., that is not account for in the IMPACTX model). The const2 term (C_{TIME}) is a constant to consider time variability between the Suzaku and NuSTAR observations. We do not multiply this constant to the scattered component and the reflection component. This is because the sizes of the scatterer and reflector are likely larger than parsec scales and hence little time variability is expected among the two observations (2005 and 2013). The normalization of the second term is linked to those in the first team so that the const3 term denotes the scattered fraction.

4. The third term represents the continuum and fluorescent lines in the reflection component from the torus plus polar dusty gas (IMPACTX). The normalization and photon index are linked to those in the first term (zcutoffpl).

5. The zgauss term represents Fe Kα fluorescent line from the broad line region (BLR). Recent high-resolution observations with XRISM suggest that the Fe Kα emission line consists of multiple components, including a narrow line originating from the torus and a broader line potentially originating from the BLR (Xrism Collaboration et al. 2024; Bogensberger et al. 2025). The equivalent width and Doppler velocity width of this component are fixed at 50 eV and 5.4×10^3 km s^{-1} (FWHM), following the XRISM result on NGC 4388 (Fujiwara et al., in preparation).

6. The two `apec` terms represent optically-thin thermal emission from the host galaxy.

4.2. *Fitting Results and Discussion*

Figure 6. The infrared SED and the best-fit IMPACT model. The black line is the total model. The red and yellow curves are the direct emission from the torus plus polar dusty gas and its scattered emission, respectively. The purple and green ones are the direct emission from the accretion disk and its scattered emission, respectively.

Our model can reproduce both the IR and broadband X-ray spectra of NGC 4388 reasonably well (within a factor of 2 for the IR SED). Table 2 summarizes the best-fit parameters; the errors on the parameters of the polar dusty gas are those derived in the second step in Section 4.1.1. The best-fit models in the IR and X-ray bands are overplotted in Figures 6 and 7, respectively. Figure 7 (b) displays the best-fit X-ray spectral model in units of EF_E (F_E is the energy flux density) with contributions from different components.

We find that the polar dusty gas in NGC 4388 has a large hydrogen column density along the radial direction ($\log N_{\rm H}^{\rm Polar}/{\rm cm}^{-2} = 23.0^{+0.0}_{-0.1}$), which are constrained by the IR SED. The torus parameters, $\sigma = 13.5^{+1.2}_{-0.1}$ degree and $\log N_{\rm H}^{\rm Equ}/{\rm cm}^{-2} = 24.5^{+0.0}_{-0.1}$.

We find that the line-of-sight absorption toward the central engine is Compton thin ($N_{\rm H}^{\rm LOS}/{\rm cm}^{-2} = 23.5^{+0.1}_{-0.1}$), confirming the previous results (Hanson et al. 1990; Iwasawa et al. 1997; Forster et al. 1999; Risaliti et al. 2002; Iwasawa et al. 2003; Beckmann et al. 2004; Shirai et al. 2008; Kamraj et al. 2017; Fukazawa et al. 2011; Miller et al. 2019; Ogawa et al. 2021).
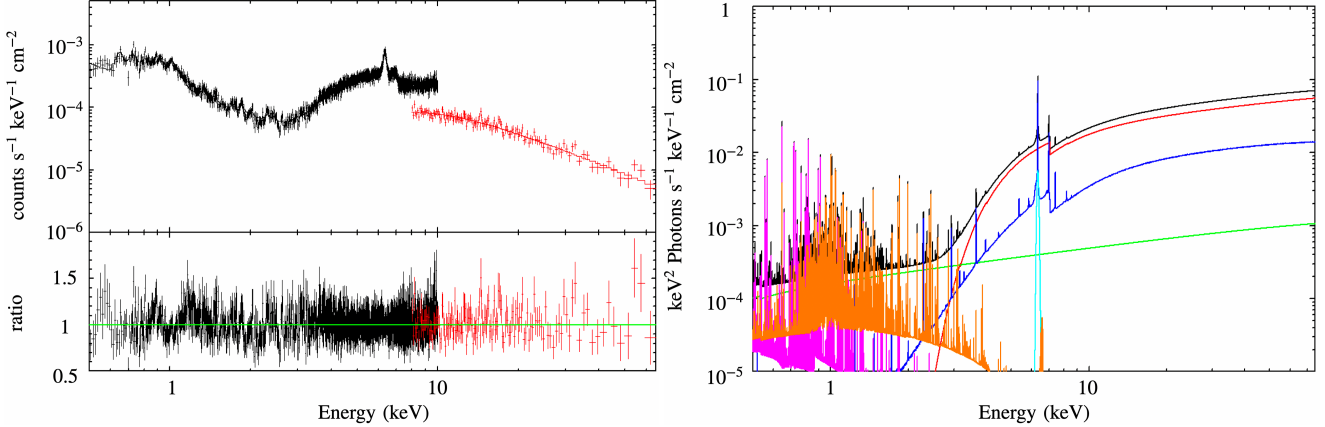
Figure 8 compares the best-fit model obtained with IMPACTX (with polar dusty gas) and that with

XCLUMPY(SKIRT) (without it). As noted, they are significantly different; the former shows an excess around 2 keV due to the reflected spectrum from the polar dusty gas. The reason why both models can reproduce the whole X-ray spectra despite of this difference is that the excess flux from the polar dusty gas can be accounted for by increasing the fraction of the "scattered component" from ionized gas (the 2nd term in equation 6). This implies that it is difficult to accurately determine the reflection component from the polar-dusty-gas using X-ray alone and complementary IR SED data are necessary. Assuming our best-fit geometry, we estimate the covering fraction by the torus and/or polar dusty gas with $\log N_{\rm H}/{\rm cm}^{-2} > 22$ to be 0.67, which is similar to that estimated from the torus-only case, 0.67, calculated according to equation 6 in Ogawa et al. (2021). This value is also consistent with the relation by Ricci et al. (2017) at the Eddington ratio of $\log \lambda_{\rm Edd} = -1.84$ (Ogawa et al. 2021), implying that the polar dusty gas is also responsible for obscuration of an AGN.
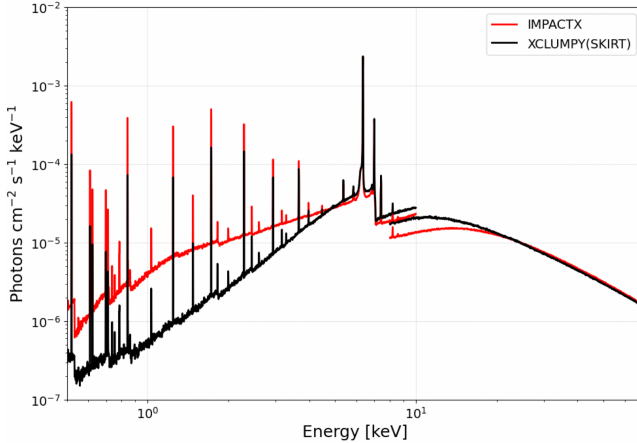
To summarize, we demonstrate that simultaneous analysis of the IR and X-ray spectra is very useful to constrain the nuclear structure including the torus and polar dusty gas. The contribution from the polar dusty gas in the X-ray spectrum can be significant, in particular when the density is high and/or opening angle is small. Hence, as pointed out by Liu et al. (2019), we have a chance to measure the outflow velocity of the polar dusty gas by detecting blue-shifted fluorescent lines in high energy resolution spectra. The torus geometry determined by assuming the torus-only geometry, as done in the previous works, are not largely affected by including the polar-dusty-gas component. However, it is possible that the covering fraction by surrounding gas may have been underestimated in objects with strong dusty outflow.

5. CONCLUSION

1. We have constructed the IMPACTX model, a generic X-ray spectral model for the reflection components from the clumpy torus and polar dusty gas in an AGN, where the same geometry as in the IMPACT model is adopted. This enables us to directly compare the X-ray and infrared results, which trace the distribution of all matter and heated dust, respectively.

2. We have confirmed that the polar dusty gas contributes to the low energy side (< 5 keV) of the X-ray spectrum, including the scattered continuum and fluorescent emission lines. Their fluxes increase with the density and decreases with the half-opening angle unless self absorption within the polar dusty gas becomes important.

3. As an example, we simultaneously analyze the IR SED and broadband X-ray spectra of NGC 4388 with the

Figure 7. (a) The broadband X-ray spectra of NGC 4388 folded with the energy response (black: Suzaku/XIS, red: NuSTAR/FPMs). The best-fit model is overplotted. (b) The best-fit model in units of EF_E (black: total, red: transmitted component, green: scattered component from ionized gas, blue: reflection component in the IMPACTX model, light blue: emission line from the BLR, orange and purple: emission from optically-thin thermal plasma.)

Figure 8. Comparison of best fit X-ray spectral models of NGC 4388 obtained with IMPACTX/IMPACT models (red) and with XCLUMPY(SKIRT) model (black).

IMPACT and IMPACTX models, respectively. We have found a solution that reproduces both data reasonably well. Comparing with the result obtained by the torus-only geometry, our new model predicts a signifi-

cantly higher flux around 2 keV due to the polar dusty gas, which is difficult to separate by using X-ray data alone. This demonstrates the importance of using both IR and X-ray data to constrain the nuclear structure.

APPENDIX

A. IR PHOTOMETRIC DATA OF NGC 4388

A.1. *IR Photometric Data*

Table A1 summarizes the photometric data of the nucleus in NGC 4388 used in this work. The HST data presented in this article were obtained from the Mikulski Archive for Space Telescopes (MAST) at the Space Telescope Science Institute. The specific observations analyzed can be accessed via doi: 10.17909/q9xf-tx22.

A.2. *X-ray Spectral Data*

Table A2 summarizes the X-ray spectral data of the nucleus in NGC 4388 used in this work.

Table 2. Best fit parameters of the IR SED and X-ray spectra of NGC 4388

Region	No.	Parameter	Best Fit Value	Units
Torus	(1)	$\log N_{\mathrm{H}}^{\mathrm{Equ}}$	$24.5^{+0.0}_{-0.1}$	cm^{-2}
	(2)	σ	$13.5^{+1.2}_{-0.1}$	degree
	(3)	i	70.0^{a}	degree
	(4)	$Z(\mathrm{Fe})$	$2.05^{+0.14}_{-0.14}$	solar
	(5)	Γ_{Suzaku}	$1.49^{+0.03}_{-0.04}$	
	(6)	Γ_{NuSTAR}	$1.72^{+0.03}_{-0.04}$	
	(7)	E_{cut}	370^{a}	keV
	(8)	N_X	$1.10^{+0.05}_{-0.09} \times 10^{-2}$	photons $\mathrm{keV}^{-1}\,\mathrm{cm}^{-2}\,\mathrm{s}^{-1}$
	(9)	f_{scat}	$1.27^{+0.10}_{-0.04} \times 10^{-2}$	
Polar dusty gas[b]	(10)	Δ_{in}	$20.0^{+0.7}_{-0.0}$	degree
	(11)	Y_{Polar}	$6.31^{+0.64}_{-0.97} \times 10^{2}$	
	(12)	$\log N_{\mathrm{H}}^{\mathrm{Polar}}$	$23.0^{+0.0}_{-0.1}$	cm^{-2}
Others	(13)	T_{apec1}	$1.20^{+0.05}_{-0.03}$	keV
	(14)	T_{apec2}	$0.31^{+0.02}_{-0.02}$	keV
	(15)	N_{apec1}	$1.84^{+0.18}_{-0.12} \times 10^{-4}$	
	(16)	N_{apec2}	$1.46^{+0.15}_{-0.15} \times 10^{-4}$	
	(17)	C_{TIME}	$0.58^{+0.08}_{-0.07}$	
	(18)	$E(B-V)$	$1.96^{+0.25}_{-0.23}$	mag
		χ^2/dof	$2080.70/1996$	

NOTE— (1) Hydrogen column density along the equatorial plane. (2) Torus angular width. (3) Inclination angle. (4) Abundance of iron relative to hydrogen. (5) Photon index for Suzaku data. (6) Photon index for NuSTAR data. (7) Cutoff energy. (8) Normalization of the intrinsic power law component at 1 keV. (9) Scattering fraction. (10) Half opening angle of the polar dusty gas. (11) Radial thickness parameter of the polar dusty gas ($R_{\mathrm{Polar}}/r_{\mathrm{in}}$). (12) Hydrogen column density of the polar dusty gas. (13), (14) Temperature of optically thin clouds. (15), (16) Normalization of the optically thin components. (17) Time variability constant. (18) Dust extinction in the host galaxy.

[a] The parameter is fixed.

[b] The errors are obtained from the fitting of the IR SED (the second step in Section 4.1).

B. XCLUMPY(SKIRT)

The XCLUMPY (Tanimoto et al. 2019) model is calculated using the MONACO (Odaka et al. 2011, 2016) framework, whereas our IMPACTX model utilizes the SKIRT framework. We note that there are differences in the atomic database and physical processes considered between MONACO and SKIRT. SKIRT adopts the photoelectric-absorption cross sections by Verner & Yakovlev (1995) and Verner et al. (1996), whereas MONACO refers to the xraylib database (Schoonjans et al. 2011). The current SKIRT code does not consider H_2 molecules, whereas MONACO does. Furthermore, the XCLUMPY model adopts the solar abundance table of Anders & Grevesse (1989), whereas our IMPACTX model uses that of Lodders et al. (2009).

To avoid any possible systematic uncertainties caused by these differences, we have also made a new table model called "XCLUMPY(SKIRT)" based on the SKIRT framework, which considers only the reflection from the torus (i.e., without the polar dusty gas). This allows us to make direct comparison with the IMPACTX model created with exactly the same conditions. Nevertheless, we note that the differences of XCLUMPY(SKIRT) from the original XCLUMPY model are sufficiently small, and do not affect our discussion.

B.1. *Fitting Results of NGC 4388*

We reanalyze the Suzaku and NuSTAR spectra using the XCLUMPY(SKIRT) model. The model is represented as follows in the XSPEC terminology:

$$\begin{aligned}
\mathrm{model} = {} & \mathsf{const1*phabs} \\
& * (\mathsf{const2*zphabs*cabs*zcutoffpl} \\
& + \mathsf{const3*zcutoffpl} + \mathsf{atable\{xclumpy\_skirt.fits\}} \\
& + \mathsf{zgauss} + \mathsf{apec1} + \mathsf{apec2}). \qquad (B1)
\end{aligned}$$

Here the tables xclumpy_skirt.fits correspond to the continuum and fluorescent lines in the reflection component from the torus. The other terms are the same as in the fitting model with IMPACTX described in Section 4.1.2. The

Table A1. Nuclear IR Photometry of NGC 4388

Telescope (1)	Instrument (2)	Filter (3)	Wavelength (4)	Flux (5)	Reference (6)
HST	NICMOS1	F110W	1.12μm	0.06±0.01	a
		F160W	1.60μm	0.7±0.1	b
VLT	SINFONI	K	2.25μm	<7.5	c
UKIRT	IRCAM3	L	3.45μm	<40	d
GTC	CanariCam	Si2	8.67μm	74±11.1	e
IRAS			25 μm	<3.57	f
			60 μm	<10.27	f
			100 μm	<17.15	f
Spitzer	IRS		4.5 μm	23.5±3.5	g
			5.5 μm	30.2±4.5	g
			18.0 μm	788.6±157.7	g
			25.0 μm	1127.1±225.4	g
			30.0 μm	1305.7±261.1	g
SOFIA	FORCAST		31.5 μm	<2040	h

NOTE— (1) Telescope name. (2) Instrument name. (3) Filter. (4) Wavelength. (5) Flux in [mJy]. (6) Reference for IR flux.

References— (a).Alonso-Herrero et al. 2003 (b).Quillen et al. 2001 (c).Burtscher et al. 2015 (d).Alonso-Herrero et al. 1998 (e).García-Bernete et al. 2016 (f).Sanders et al. 2003 (g).García-Bernete et al. 2019 (h).Fuller et al. 2016

Table A2. Observation log

Observatory (1)	Observation ID (2)	Start Date (3)	End Date (4)	Exposure (ks) (5)	Ref (6)
Suzaku	800017010	2005 Dec 24 09:04	2005 Dec 27 06:00	122	Shirai et al. 2008
NuSTAR	60061228002	2013 Dec 27 06:46	2013 Dec 27 17:26	21	Kamraj et al. 2017

NOTE— (1): observatory. (2): observation identification number. (3): start date in units of ymd. (4): end date in units of ymd. (5): exposure time in units of kiloseconds, based on good time intervals of XIS 0 for Suzaku and FPMA for NuSTAR.

fitting results are summarized in Table B3. We confirm that the parameters are consistent with those obtained by Ogawa et al. (2021) using the (original) XCLUMPY model.

REFERENCES

Aird, J., Coil, A. L., Georgakakis, A., et al. 2015, MNRAS, 451, 1892, doi: 10.1093/mnras/stv1062

Alonso-Herrero, A., Quillen, A. C., Rieke, G. H., Ivanov, V. D., & Efstathiou, A. 2003, AJ, 126, 81, doi: 10.1086/375545

Alonso-Herrero, A., Simpson, C., Ward, M. J., & Wilson, A. S. 1998, ApJ, 495, 196, doi: 10.1086/305269

Anders, E., & Grevesse, N. 1989, GeoCoA, 53, 197, doi: 10.1016/0016-7037(89)90286-X

Andonie, C., Ricci, C., Paltani, S., et al. 2022, MNRAS, 511, 5768, doi: 10.1093/mnras/stac403

Antonucci, R. R. J., & Miller, J. S. 1985, ApJ, 297, 621, doi: 10.1086/163559

Table B3. Best fit parameters of the X-ray spectra of NGC 4388 with XCLUMPY(SKIRT)

Region	No.	Parameter	Best Fit Value	Units
Torus	(1)	$\log N_{\mathrm{H}}^{\mathrm{Equ}}$	$24.0^{+0.1}_{-0.2}$	cm^{-2}
	(2)	σ	$19.3^{+9.7}_{-1.3}$	degree
	(3)	i	70.0^a	degree
	(4)	$Z(\mathrm{Fe})$	$1.83^{+0.10}_{-0.12}$	solar
	(5)	Γ_{Suzaku}	$1.48^{+0.04}_{-0.03}$	
	(6)	Γ_{NuSTAR}	$1.59^{+0.04}_{-0.02}$	
	(7)	E_{cut}	370^a	keV
	(8)	N_X	$1.03^{+0.11}_{-0.07} \times 10^{-2}$	photons $\mathrm{keV}^{-1}\,\mathrm{cm}^{-2}\,\mathrm{s}^{-1}$
	(9)	f_{scat}	$1.67^{+0.10}_{-0.10} \times 10^{-2}$	
Others	(10)	T_{apec1}	$1.19^{+0.03}_{-0.03}$	keV
	(11)	T_{apec2}	$0.31^{+0.02}_{-0.02}$	keV
	(12)	N_{apec1}	$1.65^{+0.13}_{-0.10} \times 10^{-4}$	
	(13)	N_{apec2}	$1.32^{+0.14}_{-0.16} \times 10^{-4}$	
	(14)	C_{TIME}	$0.40^{+0.06}_{-0.06}$	
		χ^2/dof	$2023.7/1974$	

NOTE— (1) Hydrogen column density along the equatorial plane. (2) Torus angular width. (3) Inclination angle. (4) Abundance of iron relative to hydrogen. (5) Photon index for Suzaku data. (6) Photon index for NuSTAR data. (7) Cutoff energy. (8) Normalization of the intrinsic power law component at 1 keV. (9) Scattering fraction. (10), (11) Temperature of optically thin clouds. (12), (13) Normalization of the optically thin components. (14)Time variability constant.

^{a}The parameter is fixed.

Arnaud, K. A. 1996, in Astronomical Society of the Pacific Conference Series, Vol. 101, Astronomical Data Analysis Software and Systems V, ed. G. H. Jacoby & J. Barnes, 17

Asmus, D. 2019, MNRAS, 489, 2177, doi: 10.1093/mnras/stz2289

Asmus, D., Hönig, S. F., & Gandhi, P. 2016, ApJ, 822, 109, doi: 10.3847/0004-637X/822/2/109

Awaki, H., Koyama, K., Inoue, H., & Halpern, J. P. 1991, PASJ, 43, 195

Baes, M., Dejonghe, H., & Davies, J. 2011, SKIRT: Stellar Kinematics Including Radiative Transfer, Astrophysics Source Code Library, record ascl:1109.003

Baloković, M., Brightman, M., Harrison, F. A., et al. 2018, ApJ, 854, 42, doi: 10.3847/1538-4357/aaa7eb

Beckmann, V., Gehrels, N., Favre, P., et al. 2004, ApJ, 614, 641, doi: 10.1086/423708

Bock, J. J., Neugebauer, G., Matthews, K., et al. 2000, AJ, 120, 2904, doi: 10.1086/316871

Bogensberger, D., Nakatani, Y., Yaqoob, T., et al. 2025, arXiv e-prints, arXiv:2507.02195, doi: 10.48550/arXiv.2507.02195

Bongiorno, A., Merloni, A., Brusa, M., et al. 2012, MNRAS, 427, 3103, doi: 10.1111/j.1365-2966.2012.22089.x

Buat, V., Mountrichas, G., Yang, G., et al. 2021, A&A, 654, A93, doi: 10.1051/0004-6361/202141797

Buchner, J., Brightman, M., Nandra, K., Nikutta, R., & Bauer, F. E. 2019, A&A, 629, A16, doi: 10.1051/0004-6361/201834771

Burtscher, L., Hönig, S., Jaffe, W., et al. 2016, in Society of Photo-Optical Instrumentation Engineers (SPIE) Conference Series, Vol. 9907, Optical and Infrared Interferometry and Imaging V, ed. F. Malbet, M. J. Creech-Eakman, & P. G. Tuthill, 99070R, doi: 10.1117/12.2231077

Burtscher, L., Orban de Xivry, G., Davies, R. I., et al. 2015, A&A, 578, A47, doi: 10.1051/0004-6361/201525817

Camps, P., & Baes, M. 2015, Astronomy and Computing, 9, 20, doi: 10.1016/j.ascom.2014.10.004

—. 2020, Astronomy and Computing, 31, 100381, doi: 10.1016/j.ascom.2020.100381

Efstathiou, A., Hough, J. H., & Young, S. 1995, MNRAS, 277, 1134, doi: 10.1093/mnras/277.3.1134

Forster, K., Leighly, K. M., & Kay, L. E. 1999, ApJ, 523, 521, doi: 10.1086/307761

Fritz, J., Franceschini, A., & Hatziminaoglou, E. 2006, MNRAS, 366, 767, doi: 10.1111/j.1365-2966.2006.09866.x

Fukazawa, Y., Hiragi, K., Mizuno, M., et al. 2011, ApJ, 727, 19, doi: 10.1088/0004-637X/727/1/19

Fuller, L., Lopez-Rodriguez, E., Packham, C., et al. 2016, MNRAS, 462, 2618, doi: 10.1093/mnras/stw1780

Furui, S., Fukazawa, Y., Odaka, H., et al. 2016, ApJ, 818, 164, doi: 10.3847/0004-637X/818/2/164

García-Bernete, I., Ramos Almeida, C., Acosta-Pulido, J. A., et al. 2016, MNRAS, 463, 3531, doi: 10.1093/mnras/stw2125

García-Bernete, I., Ramos Almeida, C., Alonso-Herrero, A., et al. 2019, MNRAS, 486, 4917, doi: 10.1093/mnras/stz1003

Gómez-Guijarro, C., González-Martín, O., Ramos Almeida, C., Rodríguez-Espinosa, J. M., & Gallego, J. 2017, MNRAS, 469, 2720, doi: 10.1093/mnras/stx1037

Hanson, C. G., Skinner, G. K., Eyles, C. J., & Willmore, A. P. 1990, MNRAS, 242, 262, doi: 10.1093/mnras/242.2.262

Hönig, S. F., Beckert, T., Ohnaka, K., & Weigelt, G. 2006, A&A, 452, 459, doi: 10.1051/0004-6361:20054622

Hönig, S. F., & Kishimoto, M. 2010, A&A, 523, A27, doi: 10.1051/0004-6361/200912676

—. 2017, ApJL, 838, L20, doi: 10.3847/2041-8213/aa6838

Hönig, S. F., Kishimoto, M., Antonucci, R., et al. 2012, ApJ, 755, 149, doi: 10.1088/0004-637X/755/2/149

Hönig, S. F., Kishimoto, M., Tristram, K. R. W., et al. 2013, ApJ, 771, 87, doi: 10.1088/0004-637X/771/2/87

Hopkins, P. F., Strauss, M. A., Hall, P. B., et al. 2004, AJ, 128, 1112, doi: 10.1086/423291

Huchra, J. P., Wyatt, W. F., & Davis, M. 1982, AJ, 87, 1628, doi: 10.1086/113254

Ichikawa, K., Packham, C., Ramos Almeida, C., et al. 2015, ApJ, 803, 57, doi: 10.1088/0004-637X/803/2/57

Ikeda, S., Awaki, H., & Terashima, Y. 2009, ApJ, 692, 608, doi: 10.1088/0004-637X/692/1/608

Isbell, J. W., Meisenheimer, K., Pott, J. U., et al. 2022, A&A, 663, A35, doi: 10.1051/0004-6361/202243271

Isbell, J. W., Ertel, S., Pott, J.-U., et al. 2025, arXiv e-prints, arXiv:2502.01840. https://arxiv.org/abs/2502.01840

Iwasawa, K., Fabian, A. C., Ueno, S., et al. 1997, MNRAS, 285, 683, doi: 10.1093/mnras/285.4.683

Iwasawa, K., Wilson, A. S., Fabian, A. C., & Young, A. J. 2003, MNRAS, 345, 369, doi: 10.1046/j.1365-8711.2003.06857.x

Jaffe, W., Meisenheimer, K., Röttgering, H. J. A., et al. 2004, Nature, 429, 47, doi: 10.1038/nature02531

Kamraj, N., Rivers, E., Harrison, F. A., Brightman, M., & Baloković, M. 2017, ApJ, 843, 89, doi: 10.3847/1538-4357/aa7563

Kormendy, J., & Ho, L. C. 2013, ARA&A, 51, 511, doi: 10.1146/annurev-astro-082708-101811

Krolik, J. H., & Begelman, M. C. 1988, ApJ, 329, 702, doi: 10.1086/166414

Kudoh, Y., Wada, K., Kawakatu, N., & Nomura, M. 2023, ApJ, 950, 72, doi: 10.3847/1538-4357/accc2b

Leftley, J. H., Tristram, K. R. W., Hönig, S. F., et al. 2018, ApJ, 862, 17, doi: 10.3847/1538-4357/aac8e5

Liu, J., Hönig, S. F., Ricci, C., & Paltani, S. 2019, MNRAS, 490, 4344, doi: 10.1093/mnras/stz2908

Lodders, K., Palme, H., & Gail, H. P. 2009, Landolt Börnstein, 4B, 712, doi: 10.1007/978-3-540-88055-4_34

López-Gonzaga, N., Burtscher, L., Tristram, K. R. W., Meisenheimer, K., & Schartmann, M. 2016, A&A, 591, A47, doi: 10.1051/0004-6361/201527590

López-Gonzaga, N., Jaffe, W., Burtscher, L., Tristram, K. R. W., & Meisenheimer, K. 2014, A&A, 565, A71, doi: 10.1051/0004-6361/201323002

Madau, P., & Dickinson, M. 2014, ARA&A, 52, 415, doi: 10.1146/annurev-astro-081811-125615

McKaig, J., Ricci, C., Paltani, S., & Satyapal, S. 2022, MNRAS, 512, 2961, doi: 10.1093/mnras/stab3178

Miller, J. M., Kammoun, E., Ludlam, R. M., et al. 2019, ApJ, 884, 106, doi: 10.3847/1538-4357/ab3e05

Murphy, K. D., & Yaqoob, T. 2009, MNRAS, 397, 1549, doi: 10.1111/j.1365-2966.2009.15025.x

Nenkova, M., Sirocky, M. M., Ivezić, Ž., & Elitzur, M. 2008a, ApJ, 685, 147, doi: 10.1086/590482

Nenkova, M., Sirocky, M. M., Nikutta, R., Ivezić, Ž., & Elitzur, M. 2008b, ApJ, 685, 160, doi: 10.1086/590483

Odaka, H., Aharonian, F., Watanabe, S., et al. 2011, ApJ, 740, 103, doi: 10.1088/0004-637X/740/2/103

Odaka, H., Yoneda, H., Takahashi, T., & Fabian, A. 2016, MNRAS, 462, 2366, doi: 10.1093/mnras/stw1764

Ogawa, S., Ueda, Y., Tanimoto, A., & Yamada, S. 2021, ApJ, 906, 84, doi: 10.3847/1538-4357/abccce

Packham, C., Radomski, J. T., Roche, P. F., et al. 2005, ApJL, 618, L17, doi: 10.1086/427691

Paltani, S., & Ricci, C. 2017, A&A, 607, A31, doi: 10.1051/0004-6361/201629623

Pier, E. A., & Krolik, J. H. 1992, ApJ, 401, 99, doi: 10.1086/172042

Prevot, M. L., Lequeux, J., Maurice, E., Prevot, L., & Rocca-Volmerange, B. 1984, A&A, 132, 389

Quillen, A. C., McDonald, C., Alonso-Herrero, A., et al. 2001, ApJ, 547, 129, doi: 10.1086/318328

Radomski, J. T., Piña, R. K., Packham, C., et al. 2003, ApJ, 587, 117, doi: 10.1086/367612

Ramos Almeida, C., & Ricci, C. 2017, Nature Astronomy, 1, 679, doi: 10.1038/s41550-017-0232-z

Ricci, C., & Paltani, S. 2023, ApJ, 945, 55, doi: 10.3847/1538-4357/acb5a6

Ricci, C., Trakhtenbrot, B., Koss, M. J., et al. 2017, Nature, 549, 488, doi: 10.1038/nature23906

Risaliti, G., Elvis, M., & Nicastro, F. 2002, ApJ, 571, 234, doi: 10.1086/324146

Salvato, M., Hasinger, G., Ilbert, O., et al. 2009, ApJ, 690, 1250, doi: 10.1088/0004-637X/690/2/1250

Sanders, D. B., Mazzarella, J. M., Kim, D. C., Surace, J. A., & Soifer, B. T. 2003, AJ, 126, 1607, doi: 10.1086/376841

Schartmann, M., Meisenheimer, K., Camenzind, M., et al. 2008, A&A, 482, 67, doi: 10.1051/0004-6361:20078907

Schartmann, M., Wada, K., Prieto, M. A., Burkert, A., & Tristram, K. R. W. 2014, MNRAS, 445, 3878, doi: 10.1093/mnras/stu2020

Schlegel, D. J., Finkbeiner, D. P., & Davis, M. 1998, ApJ, 500, 525, doi: 10.1086/305772

Schoonjans, T., Brunetti, A., Golosio, B., et al. 2011, Spectrochimica Acta - Part B: Atomic Spectroscopy, 66, 776, doi: 10.1016/j.sab.2011.09.011

Shirai, H., Fukazawa, Y., Sasada, M., et al. 2008, PASJ, 60, S263, doi: 10.1093/pasj/60.sp1.S263

Siebenmorgen, R., Haas, M., Krügel, E., & Schulz, B. 2005, A&A, 436, L5, doi: 10.1051/0004-6361:200500109

Sorce, J. G., Tully, R. B., Courtois, H. M., et al. 2014, MNRAS, 444, 527, doi: 10.1093/mnras/stu1450

Stalevski, M., Asmus, D., & Tristram, K. R. W. 2017, MNRAS, 472, 3854, doi: 10.1093/mnras/stx2227

Stalevski, M., Fritz, J., Baes, M., Nakos, T., & Popović, L. Č. 2012, MNRAS, 420, 2756, doi: 10.1111/j.1365-2966.2011.19775.x

Stalevski, M., Ricci, C., Ueda, Y., et al. 2016, MNRAS, 458, 2288, doi: 10.1093/mnras/stw444

Stalevski, M., Tristram, K. R. W., & Asmus, D. 2019, MNRAS, 484, 3334, doi: 10.1093/mnras/stz220

Tanimoto, A., Ueda, Y., Odaka, H., et al. 2019, ApJ, 877, 95, doi: 10.3847/1538-4357/ab1b20

Tristram, K. R. W., Burtscher, L., Jaffe, W., et al. 2014, A&A, 563, A82, doi: 10.1051/0004-6361/201322698

Ueda, Y., Akiyama, M., Hasinger, G., Miyaji, T., & Watson, M. G. 2014, ApJ, 786, 104, doi: 10.1088/0004-637X/786/2/104

Vander Meulen, B., Camps, P., Stalevski, M., & Baes, M. 2023, A&A, 674, A123, doi: 10.1051/0004-6361/202245783

Vander Meulen, B., Camps, P., Tsujimoto, M., & Wada, K. 2024, A&A, 688, L33, doi: 10.1051/0004-6361/202451370

Verner, D. A., Ferland, G. J., Korista, K. T., & Yakovlev, D. G. 1996, ApJ, 465, 487, doi: 10.1086/177435

Verner, D. A., & Yakovlev, D. G. 1995, A&AS, 109, 125

Wada, K., Schartmann, M., & Meijerink, R. 2016, ApJL, 828, L19, doi: 10.3847/2041-8205/828/2/L19

Willingale, R., Starling, R. L. C., Beardmore, A. P., Tanvir, N. R., & O'Brien, P. T. 2013, MNRAS, 431, 394, doi: 10.1093/mnras/stt175

Xrism Collaboration, Audard, M., Awaki, H., et al. 2024, ApJL, 973, L25, doi: 10.3847/2041-8213/ad7397

Yamada, S., Ueda, Y., Herrera-Endoqui, M., et al. 2023, ApJS, 265, 37, doi: 10.3847/1538-4365/acb349